Chinese Chemical Letters 36 (2025) 109763

Contents lists available at ScienceDirect

Chinese Chemical Letters

journal homepage: www.elsevier.com/locate/cclet

Biomimetic nanoplatform integrates FRET-enhanced photodynamic therapy and chemotherapy for cascaded revitalization of the tumor immune microenvironment in OSCC

Wenbin Zhou[a,b,c,1], Yafei Gao[a,b,c,1], Xinyu Feng[a,b,c], Yanqing Zhang[a,b,c], Cong Yang[a,b,c], Lanxi He[a,b,c], Fenghe Zhang[a,b,c,*], Xiaoguang Li[d,*], Qing Li[a,b,c,*]

[a] School and Hospital of Stomatology, Cheeloo College of Medicine, Shandong University, Ji'nan 250012, China
[b] China & Shandong Key Laboratory of Oral Tissue Regeneration, Ji'nan 250012, China
[c] China & Shandong Engineering Laboratory for Dental Materials and Oral Tissue Regeneration, Ji'nan 250012, China
[d] Department of Stomatology, Shandong Provincial Hospital Affiliated to Shandong First Medical University, Ji'nan 250021, China

ARTICLE INFO

Article history:
Received 16 February 2024
Revised 9 March 2024
Accepted 11 March 2024
Available online 12 March 2024

Keywords:
Biomimetic nanoplatform
UCNP-PDT
Chemotherapy
TIME
OSCC

ABSTRACT

Immunotherapy offers significant potential but is often hampered by the immunosuppressive environment in oral squamous cell carcinoma (OSCC). To address this, we propose an enhanced immunotherapeutic strategy that revitalizes the tumor immune microenvironment (TIME) in OSCC by integrating upconversion-based photodynamic therapy (PDT) with chemotherapy. Using a red blood cell membrane-inspired biomimetic nanoplatform, our approach concurrently delivers chlorin e6@upconversion nanoparticles (Ce6@UCNP) and doxorubicin (DOX). By leveraging fluorescence resonance energy transfer (FRET) for 980 nm to 660 nm upconversion excitation, we address challenges such as limited tissue penetration and tissue damage, as well as nanoplatform issues including immunogenicity and targeting inaccuracy Our integrated approach enhances PDT and chemotherapy with the goal of transforming immunologically "cold" tumors into "hot" ones through a cascaded therapy, thereby revitalizing the tumor immune microenvironment in OSCC.

Oral squamous cell carcinoma (OSCC) presents challenges for traditional therapies, including surgery, radiotherapy, and chemotherapy [1]. Surgical resection, the preferred treatment, is often impeded by late diagnosis and complex oral anatomy, resulting in uncertain margins and increased risks of recurrence and metastasis [2]. Adjuvant therapies such as chemotherapy have limited effectiveness, suffer from adverse effects [3,4], and face the challenge of drug resistance development [5–7]. In contrast, immunotherapy has marked a transformative phase in cancer treatment with notable successes [8,9]. However, the effectiveness of immunotherapy is dependent mainly on T-cell infiltration in tumors [10]. Unfortunately, this condition is rarely met in the immunosuppressive microenvironment of OSCC, which restricts T-cell activation and penetration [11,12].

Therefore, inducing immunogenic cell death (ICD) effectively counteracts the tumor's immunosuppressive state and remodels its immune microenvironment [13]. ICD releases tumor antigens and damage-associated molecular patterns (DAMPs), rejuvenating the immune response and enhancing T-cell activation, proliferation, and infiltration [14–16]. This transformation changes "cold" tumors into "hot" ones [17,18]. It is noteworthy that frontline agents, such as the chemotherapeutic doxorubicin (DOX) and the photosensitizer chlorin e6 (Ce6), are potent ICD inducers [19,20]. This research proposes a novel approach that combines photodynamic therapy (PDT) using Ce6 with chemotherapy employing DOX to reshape the tumor immune landscape, effectively inhibiting OSCC progression and metastasis. Integrating nanoplatform with PDT and chemotherapy using these key agents aims to enhance anticancer efficacy, reduce monotherapy-related toxicities, and overcome chemotherapy resistance. However, the clinical application of PDT faces challenges including limited tissue penetration, tissue damage caused by visible light, significant toxicity from experimental photosensitizers, and complications related to nanoplatforms such as immunogenicity, rapid clearance, and inaccurate targeting [21–23].

To address these challenges, we employed Nanoplatform to co-deliver key clinical agents, Ce6, DOX and upconversion nanoparti-

* Corresponding authors.
E-mail addresses: zfengh@sdu.edu.cn (F. Zhang), xiaopa3084@126.com (X. Li), lq580202@sdu.edu.cn (Q. Li).
[1] These authors contributed equally to this work.

https://doi.org/10.1016/j.cclet.2024.109763
1001-8417/

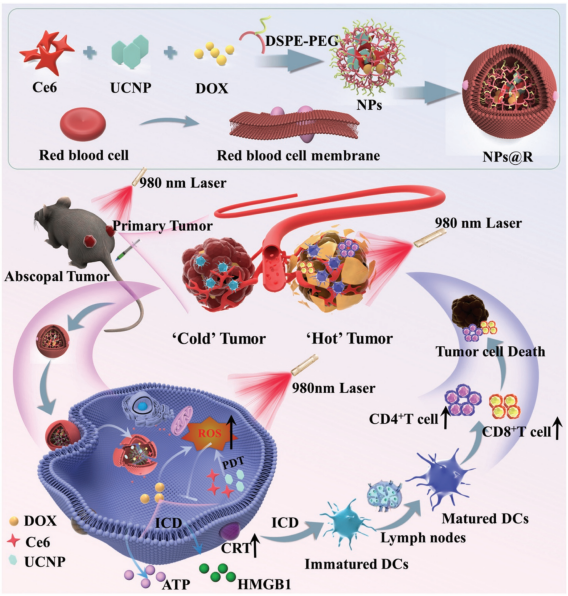

Scheme 1. This diagram illustrates the innovative design of NPs@R, which combines PDT-UCNP and chemotherapy to treat OSCC through a cascading treatment approach. Nanoplatform is integrated with RBC membranes to facilitate the co-delivery of Ce6@UCNP and DOX. This strategic combination significantly enhances ICD and transforms immunologically dormant "cold" tumors into immunologically active "hot" tumors, revitalizing the TIME.

cles (UCNP), enabling simultaneous UCNP-PDT and chemotherapy for OSCC treatment. This strategy addresses common limitations of small molecule drugs, such as poor tumor accumulation and short retention times, by enabling targeted delivery and reducing side effects. Utilizing upconversion and fluorescence resonance energy transfer (FRET), the low-energy near-infrared light at 908 nm is effectively transformed into high-energy visible light at 660 nm. This synergy between UCNP and Ce6 markedly increases Ce6's therapeutic depth in tumor tissues, resulting in enhanced tissue penetration [24,25]. We utilized red blood cell membranes to construct a biomimetic nanoplatform, which presents an innovative approach that improves systemic circulation and tumor targeting [26,27]. The absence of nuclei and organelles in mature red blood cells allows for easier membrane extraction and purification. This makes the biomimetic nanoplatform strategy particularly advantageous for clinical applications compared to other cell membrane-mimicking systems [28,29].

This study uses a biomimetic nanoplatform based on red blood cell membranes to co-deliver optimized Ce6@UCNP and DOX. The approach increases reactive oxygen species (ROS) generation from Ce6@UCNP and reinforces DOX's chemotherapeutic effect, compensating for UCNP-PDT's reduced efficacy in oxygen-deficient tumor microenvironment [30]. The increase in ROS levels triggers ICD, enabling a combined strategy of UCNP-PDT and chemotherapy to induce apoptosis in OSCC cells and convert immunologically "cold" tumors into "hot" ones, thereby revitalizing the TIME (Scheme 1). This innovative approach shows promise as a therapeutic option, with the goal of overcoming the limitations of current OSCC treatments, improving therapeutic outcomes, and reducing the risk of recurrence and metastasis.

1,2-Distearoyl-*sn*–glycero-3-phosphoethanolamine-*N*-poly(ethylene glycol)-UCNP (DSPE-PEG-UCNP) exhibits narrow emission bands at 530–560 and 645–675 nm under 980 nm excitation, with an emission peak at 660 nm coinciding with the absorption peak of Ce6, suggesting potential energy resonance transfer between UCNP and Ce6 (Fig. 1A). Since the excitation wavelength of Ce6 around 660 nm has limited penetration, hindering effective tumor depth reach, 980 nm laser excitation of UCNP can efficiently activate Ce6 for PDT. Dynamic light scattering (DLS) was used to determine the sizes of the prepared Nanoplatform, which showed average diameters of 132.2 ± 4.02 nm for nanoparticles (NPs) (Fig. S1 in Supporting information) and 146.4 ± 5.35 nm for NPs@R (Fig. 1B). Transmission electron microscope (TEM) imaging showed that NPs@R (Fig. 1C) maintained regular spherical shapes with a core-shell structure, slightly larger than NPs (Fig. S2 in Supporting information), indicating successful cell membrane encapsulation. Zeta potential evaluations revealed values of −3.67 ± 0.98 mV for NPs and −13.9 ± 1.9 mV for NPs@R (Fig. 1D), reflecting the favorable size and charge properties of the nanomedicine. Stability evaluations revealed no significant size variation for both NPs@R (Fig. 1E) and NPs in 10% fetal bovine serum (FBS) solution over seven days (Fig. S3 in Supporting information), confirming the stability of the nanomedicine and consistent accumulation at the tumor site for enhanced therapeutic efficacy. Western blot (Fig. 1F) confirmed similar levels of CD44 and CD47 on both the red blood cell (RBC) membrane and surface of NPs@R, with negligible loss after encapsulation, demonstrating successful membrane encapsulation. The RBC membrane (RCM)-coated nanomedicine can evade macrophage phagocytosis through the "don't eat me" signal of CD47, which significantly prolongs the circulation time. Ultraviolet–visible (UV–vis) spectroscopy (Fig. S4 in Supporting information) verified the effective loading of DOX and Ce6, with loading efficiencies of 10.4% and encapsulation rates of 64.3% for DOX and a loading efficiency of 8.3% for Ce6.

RCM-encapsulated nanoplatform shows potential to evade macrophage-mediated elimination, prolong blood circulation, and enhance drug targeting to tumors. Fig. 2A shows that after 4 h of co-culture, endosomal escape was more efficient in the NPs@R group than in the NPs group, suggesting that RCM encapsulation enhances nanomedicine uptake by OSCC cells. The cell counting kit-8 (CCK-8) assay evaluated the inhibitory effects on scc7 cell proliferation, which showed concentration-dependent efficacy in Fig. S5 (Supporting information). Laser-treated groups showed a significantly higher cell inhibition rate than non-laser-treated groups, highlighting the efficacy of UCNP-PDT against OSCC. The half maximal inhibitory concentration (IC_{50}) values were 0.43 μg/mL for the DOX group, 0.17 μg/mL for the NPs group, and 0.13 μg/mL for the NPs@R group, demonstrating that RCM encapsulation enhances drug stability and tumor cell uptake, which significantly improves OSCC inhibition with the combination of DOX and UCNP-PDT. Fig. 2B shows that the laser-treated groups exhibited increased levels of ROS, with the effect particularly pronounced in the RBC-mimicking NPs@R(+) group. UCNP-PDT is effective in generating significant amounts of ROS, which in turn enhances the chemotherapeutic effect of DOX. This enhanced chemotherapeutic response compensates for the limited efficacy of PDT in oxygen-deprived tumors. This cascaded therapy resulted in significant apoptosis in scc7 cells as shown in Fig. S5. In addition, the increased ROS levels are more likely to induce ICD, thereby rejuvenating the tumor immune microenvironment. After 12 h of co-culture of scc7 cells with different nanomedicine formulations, calreticulin (CRT) fluorescence staining (Fig. 2C) showed minimal CRT expression on the cell membranes of NPs(-) and NPs@R(-) groups, indicating the ability of DOX to induce ICD in OSCC. Enhanced CRT expression was observed in the laser-treated groups, particularly in the NPs@R(+) group, suggesting that RCM encapsulation facilitates nanomedicine uptake by tumor cells. Adenosine triphosphate (ATP) release (Fig. 2D) and high-mobility group box 1 protein (HMGB1) release (Fig. 2E) were more pronounced in the NPs@R group after laser treatment, indicating the combined effect of PDT and DOX in inducing significant ICD in tumor cells. The subsequent ICD leads to dendritic cell (DC) maturation and antigen presentation. For flow cytometry analysis, DCs were co-cultured

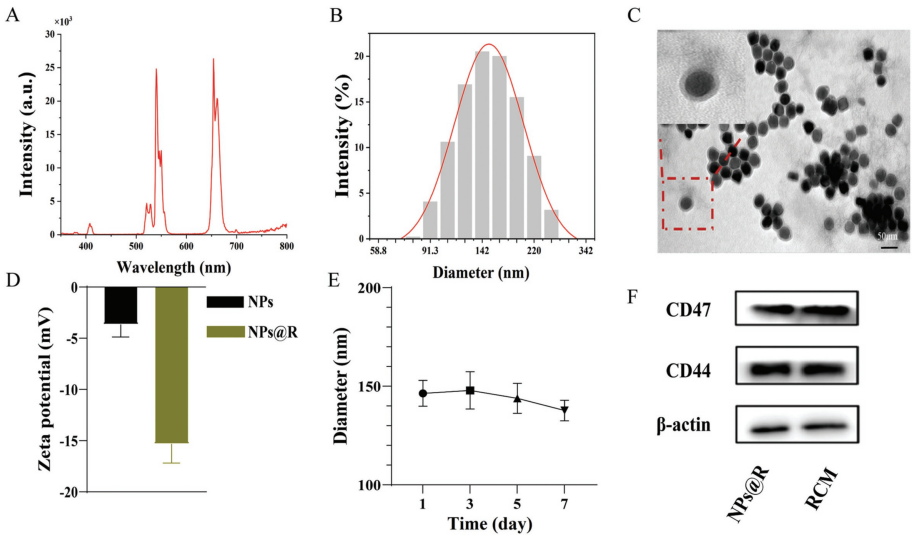

Fig. 1. Characterization of nanoplatform. (A) The emission spectrum of UCNP under 980 nm excitation. (B) Particle size distribution of NPs@R. (C) TEM image of NPs@R (scale bar: 50 nm). (D) Zeta potential of nanoplatform. (E) Stability assessment of NPs@R over 7 days. (F) Western blot analysis for CD47 and CD44 in NPs@R and RCM, with β-actin as a control. Data are represented as mean ± SD ($n = 3$).

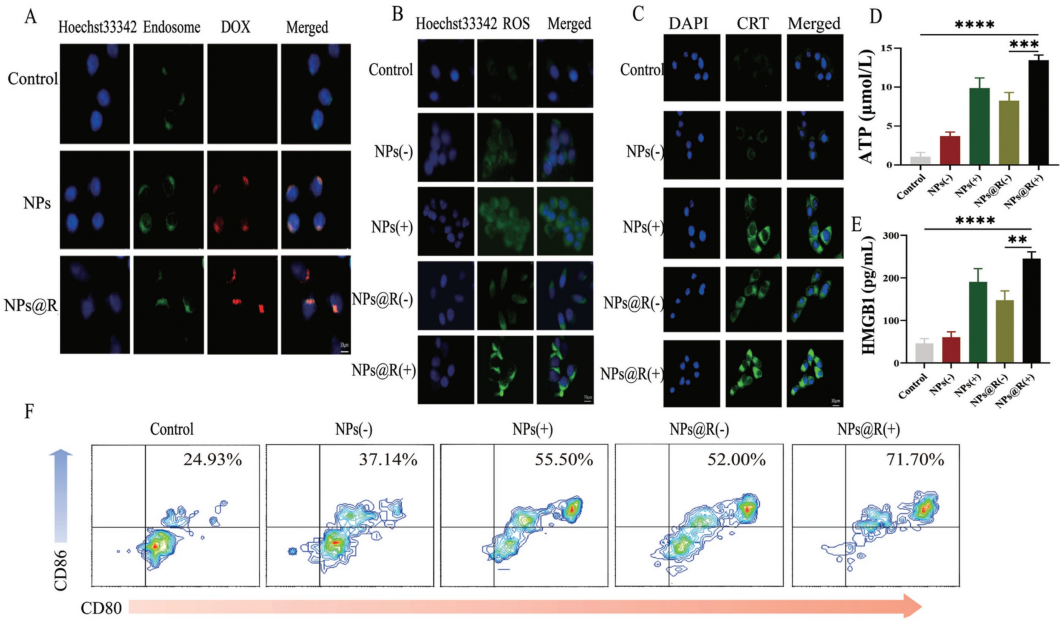

Fig. 2. *In vitro* cellular experiments. (A) Endosomal escape experiments of control, NPs, and NPs@R. (B) ROS release after co-culturing different drug formulations with scc7 cells for 4 h. (C) Detection of CRT translocation on the cell membrane surface after co-culturing different drug formulations with scc7 cells. (D) ATP release after co-culturing different drug formulations with scc7 cells. (E) HMGB1 release after co-culturing different drug formulations with scc7 cells. (F) DC maturation after co-culturing drug treated scc7 with DC. Data are represented as mean ± SD ($n = 3$). $^{**}P < 0.01$, $^{***}P < 0.001$, $^{****}P < 0.0001$. Scale bar: 30 μm.

with scc7 cells treated with the drug formulations. The results showed a DC maturation rate of 24.93% in the control group, 37.14% in the non-irradiated NPs group (NPs(-)), 55.50% in the irradiated NPs group (NPs(+)), 52.00% in the non-irradiated biomimetic NPs group (NPs@R(-)), and 71.70% in the irradiated biomimetic NPs group (NPs@R(+)). These results indicated that drug-treated scc7 cells significantly promoted DC maturation, and the effect was more pronounced in the irradiated groups. Notably, the group treated with erythrocyte membrane-mimicking nanoparticles and exposed to laser irradiation (NPs@R(+)) showed the most substantial effect, indicating the maximal restoration of tumor cell immunogenicity (Fig. 2F). This suggests that the NPs@R(+) group effectively induces ICD, promotes DC maturation and enhances antigen presentation, thereby recruiting T cells to the tumor and improving the tumor immune environment.

After confirming the antitumor efficacy of the nanomedicine *in vitro*, we extended our investigation to C3H mice to evaluate its biological performance. All *in vivo* experiments received approval from the Ethics Committee of Shandong University School of Stomatology (No. 20230321). Analysis of DOX concentration in mouse blood, as shown in Fig. S6 (Supporting information), revealed a reduced fluorescence decay rate in the NPs@R group compared to both NPs and free drug counterparts, with 29.5% ± 4.06% of DOX remaining detectable after 24 h. This result underscores the enhanced retention and circulation afforded by the RCM integration in NPs@R, highlighting the ability of RBC-mimetic nanoparticles

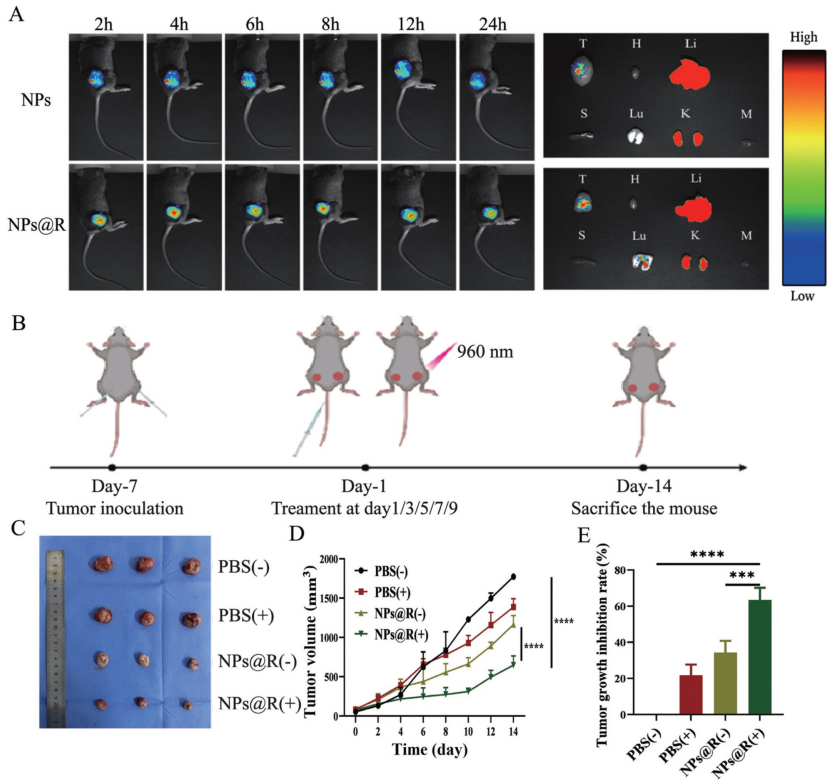

Fig. 3. *In vivo* drug distribution and antitumor experiments. (A) Fluorescent images at the tumor site and organ distribution post-treatment (T: tumor, H: heart, Li: liver, S: spleen, Lu: lung, K: kidney, M: muscle). (B) Tumor treatment protocol. (C) Distant tumor imaging. (D) Volume changes in distant tumor. (E) Distant tumor inhibition rates. Data are represented as mean ± SD ($n = 3$). $^{***}P < 0.001$, $^{****}P < 0.0001$.

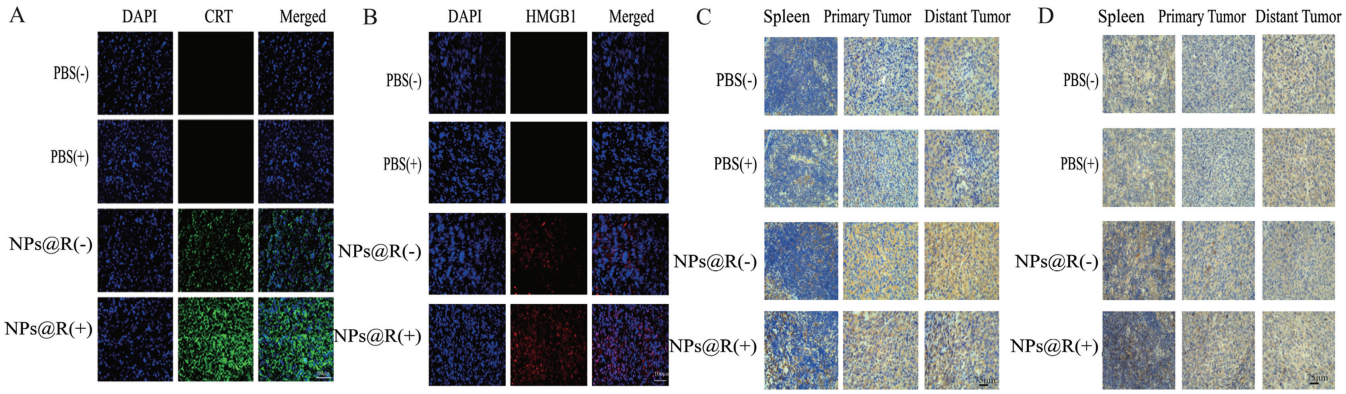

Fig. 4. Immunofluorescence and immunohistochemical staining. (A) CRT and (B) HMGB1 expression *in situ* tumor tissues. Scale bar: 100 μm. (C) $CD4^+$ and (D) $CD8^+$ expression in spleen, *in situ*, and distant tumor tissues. Scale bar: 75 μm.

to preserve surface protein functionality, evade immune surveillance, and achieve targeted drug delivery to tumors. *In vivo* imaging system experiments (Fig. 3A) revealed significant drug accumulation at the tumor site, demonstrating the effective tumor targeting capability of the nanoplatform. The NPs@R group showed a peak in fluorescence intensity at 4 h after administration, indicating improved drug delivery. A significant decrease in fluorescence was observed after 8 h, especially in the NPs group, indicating the prolonged circulation enabled by the RCM camouflage. Predominant drug localization in liver and kidney tissues indicated primary elimination routes, with negligible accumulation in heart, spleen and muscle, suggesting mitigation of DOX-related side effects. Using a dual tumor model in C3H mice (Fig. 3B), a significant reduction in tumor growth rate was observed in the NPs@R(+) group, achieving an inhibition rate of 67.4%, twice the efficacy observed in the non-laser group. This underscores the superior tumor control executed by the synergistic application of UCNP-PDT and DOX (Figs. S7–S9 in Supporting information). The growth inhibition of distant tumors also showed a slowing pattern (Figs. 3C–E), with an inhibition rate of 63.5% in the NPs@R(+) group, indicating the ability of the treatment to induce an immune response against metastatic tumors. Mouse weight tracking throughout the treatment period (Fig. S10 in Supporting information) showed no significant fluctuations, confirming the minimal toxicity profile of the nanomedicine.

At the end of treatment, hematoxylin-eosin (H&E) staining of harvested tissues (Fig. S11 in Supporting information) showed no adverse changes, confirming the biosafety of the nanomedicine. Immunofluorescence staining (Figs. 4A and B) revealed increased levels of calreticulin (CRT) and high mobility group box 1 (HMGB1)

in tumor tissues, predominantly in the NPs@R(+) group, consistent with *in vitro* results and validating ICD initiation by treatment. Immunohistochemical assessments (Figs. 4C and D) revealed increased infiltration of $CD4^+$ T and $CD8^+$ T cells in the NPs@R group, especially after laser treatment, indicating improved antigen presentation and T cell recruitment, effectively turning "cold" tumors into "hot" ones and enhancing the efficacy of immunotherapy.

We have devised a cutting-edge biomimetic Nanoplatform capable of rejuvenating the TIME in OSCC. Our method merges UCNP-PDT with chemotherapy, driving significant apoptosis in OSCC cells through a cascading treatment strategy. This technique substantially boosts ICD, effectively converting immunologically inert "cold" tumors into active "hot" ones, thus reinvigorating the tumor's immune milieu. This innovative approach represents a significant advancement in OSCC therapy, holding promise for improved patient outcomes and a reduction in the likelihood of tumor relapse and metastasis.

Declaration of competing interest

The authors declare that they have no known competing financial interests or personal relationships that could have appeared to influence the work reported in this paper.

Acknowledgments

This work was supported by the National Natural Science Foundation of China (No. 81802709); the Shandong Provincial Natural Science Foundation, China (Nos. ZR2023MH230, ZR2023MH096); the Shandong Provincial Postdoctoral Innovative Talents Funded Scheme; Plan of Young Scholars of Shandong University.

Supplementary materials

Supplementary material associated with this article can be found, in the online version, at doi:10.1016/j.cclet.2024.109763.

References

[1] A.C. Chi, T.A. Day, B.W. Neville, CA Cancer J. Clin. 65 (2015) 401–421.
[2] R.W. Gao, N.T. Teraphongphom, N.S. van den Berg, et al., Cancer Res. 78 (2018) 5144–5154.
[3] X. You, L. Wang, J. Zhang, et al., Chin. Chem. Lett. 34 (2023) 107720.
[4] H. Hu, Z. Zhang, Y. Fang, et al., Chin. Chem. Lett. 34 (2023) 107953.
[5] C.S. Huang, Q.C. Xu, C. Dai, et al., ACS Nano 15 (2021) 14744–14755.
[6] L. Wang, X. Huang, X. You, et al., Signal Transduct. Target. Ther. 5 (2020) 196.
[7] M. Hao, F. Song, X. Du, et al., Cancer Lett. 359 (2015) 1–8.
[8] L. Galluzzi, J. Humeau, A. Buqué, et al., Nat. Rev. Clin. Oncol. 17 (2020) 725–741.
[9] G. Morad, B.A. Helmink, P. Sharma, et al., Cell 184 (2021) 5309–5337.
[10] P. Jiang, S. Gu, D. Pan, et al., Nat. Med. 24 (2018) 1550–1558.
[11] Y. Liu, Z. Sun, Theranostics 11 (2021) 5365–5386.
[12] J. Galon, D. Bruni, Nat. Rev. Drug Discov. 18 (2019) 197–218.
[13] A.D. Garg, P. Agostinis, Immunol. Rev. 280 (2017) 126–148.
[14] T. He, L. Wang, S. Gou, et al., ACS Nano 17 (2023) 9953–9971.
[15] C. Huang, B. Lin, C. Chen, et al., Adv. Mater. 34 (2022) e2207593.
[16] K. Hayashi, F. Nikolos, Y.C. Lee, et al., Nat. Commun. 11 (2020) 6299.
[17] S. Zhang, J. Wang, Z. Kong, et al., Biomaterials 282 (2022) 121433.
[18] Y. Lu, Y. Wang, W. Liu, et al., Biomaterials 296 (2023) 122089.
[19] S. Yang, M.K. Shim, W.J. Kim, et al., Biomaterials 272 (2021) 120791.
[20] H. Xiao, X. Li, B. Li, et al., Small 19 (2023) e2300280.
[21] J. Xie, Y. Wang, W. Choi, et al., Chem. Soc. Rev. 50 (2021) 9152–9201.
[22] B. Sun, J.Y. Teo, J. Wu, et al., Acc. Chem. Res. 56 (2023) 1143–1155.
[23] W. Yu, X. He, Z. Yang, et al., Biomaterials 217 (2019) 119309.
[24] L. Pang, X. Tang, L. Yao, et al., Chem. Sci. 14 (2023) 3070–3075.
[25] F. Jin, J. Qi, M. Zhu, et al., ACS Appl. Mater. Interfaces 12 (2020) 32372–32387.
[26] W. Liu, M. Ruan, Y. Wang, et al., Small 14 (2018) e1801754.
[27] J. Xiong, M. Wu, J. Chen, et al., ACS Nano 15 (2021) 19756–19770.
[28] Q. Jiang, Z. Luo, Y. Men, et al., Biomaterials 143 (2017) 29–45.
[29] P.H.D. Nguyen, M.K. Jayasinghe, A.H. Le, et al., ACS Nano 17 (2023) 5187–5210.
[30] Y. Chen, Y. Yang, S. Du, et al., ACS Appl. Mater. Interfaces 15 (2023) 35884–35894.